

## Original article

# Effects of pore connectivity and water saturation on matrix permeability of deep gas shale

Jiale Zhao<sup>1,2</sup>, Mengdi Sun<sup>1,2</sup>\*, Zhejun Pan<sup>1</sup>, Bo Liu<sup>1</sup>, Mehdi Ostadhassan<sup>1</sup>, Qinhong Hu<sup>3</sup>

<sup>1</sup>Key Laboratory of Continental Shale Hydrocarbon Accumulation and Efficient Development, Ministry of Education, Northeast Petroleum University, Daqing 163318, P. R. China

<sup>2</sup>Key Laboratory of Tectonics and Petroleum Resources, Ministry of Education, China University of Geosciences, Wuhan 430074, P. R. China

<sup>3</sup>Department of Earth and Environment Sciences, University of Texas at Arlington, Arlington, TX 76019, USA

### Keywords:

Matrix permeability  
pore structure  
water vapor adsorption  
deep shale  
Wufeng-Longmaxi shale

### Cited as:

Zhao, J., Sun, M., Pan, Z., Liu, B., Ostadhassan, M., Hu, Q. Effects of pore connectivity and water saturation on matrix permeability of deep gas shale. *Advances in Geo-Energy Research*, 2022, 6(1): 54-68.

<https://doi.org/10.46690/ager.2022.01.05>

### Abstract:

Shale matrix permeability is an important indicator for evaluating gas transport and production. However, the effects of pore connectivity and water saturation on the matrix permeability in deep gas shales have not been adequately studied. In this study, the permeability of deep shales in the Yichang area of the Middle Yangtze was characterized using three methods. These included the determination of apparent permeability in different directions via pulse-decay, also matrix permeability obtained via the Gas Research Institute method, and the connected pore network permeability via the mercury injection capillary pressure technique. The results revealed a significant difference between the horizontal and vertical permeability of deep shales. The smaller the size of the multiple connected pore network, the larger was the effective tortuosity and the lower the permeability. Comparison of the three permeabilities and combined microscopic observations revealed that microfractures and laminae were the dominant gas transport channels. Importantly, the matrix permeability decreased exponentially with increasing water saturation, with water vapor adsorption experiments revealing that water occupation of pores and pore-throat spaces smaller than 10 nm in diameter was the main reason for this decrease in matrix permeability. Collectively, proposed method of evaluating effective permeability with an index for shale gas reservoirs is significant for sweet spot selection and production prediction of shale gas reservoirs around the globe.

## 1. Introduction

China's shale gas has been successfully developed and has become the preferred target for gas storage and production, with annual shale gas production exceeding 20 billion cubic meters in 2020 (Zou et al., 2021). However, while the production of shale gas in China has been growing steadily, current production is mainly from formations at relatively shallower depths. It is important to note that while studies have noted the valuable resource prospect of deep shale gas in China as being linked to an abundant occurrence and wide distribution (Li et al., 2021), controls behind the gas transport processes has not been fully understood due to the imperfections of effective

matrix permeability evaluation methods for such reservoirs.

Based on what was said above, shale with a burial depth greater than 3500 m is usually defined as deep shale (He et al., 2019). Some differences were found between deep shales and the shallower ones in correlation between porosity and depth, permeability, pore geometry and connectivity. Studies have found that deep shales do not follow the decreasing porosity with increasing depth of burial pattern (Zhang et al., 2021). This means, many deep shales would belong to the strata that is overpressured. The overpressured nature of these formations can offset the mechanical compaction of the pore space from the overlying formation pressure to a certain extent, slowing down or even changing the decreasing trend

of the pore space with burial depth (Duan et al., 2018). Thus, many overpressured deep shales have the equivalent porosity as the shallower ones. However, even though the porosity is comparable, permeability in the deeper ones is significantly lower. In this regard, because of the burial depth, microfractures are poorly developed in the deeper ones. Moreover, being overpressured, micropores of deep shale are very well developed and the pore shape is rounded-elliptical (Guo et al., 2020). All these complications in the development of pore space in the deep shale matrix makes it necessary to study and evaluate their permeability.

Among the many factors affecting the permeability of shale, pore connectivity and water content are two critical parameters. In recent years, many studies have been conducted on the relationship between pore connectivity and permeability in shallow shale (Qu et al., 2016; Sun et al., 2017; Achang et al., 2019; Davudov et al., 2020). The relationship between pore connectivity and permeability through the assessing the numbers of pores and pore throats has also been discussed (Qu et al., 2016). Davudov et al. (2020) successfully characterized the matrix permeability and pore connectivity relationship of the Eagle Ford Shale using a three-dimensional reconstruction technique. Some researchers believe that fracture permeability decreases owing to high-pressure conditions as depth increases (Cui et al., 2018; Tan et al., 2019). Poor pore network connectivity within the shale matrix is another major reason for the decrease in permeability (Davudov et al., 2020; Sun et al., 2020). With the large-scale development of deep shale, the relationship between deep shale permeability and pore connectivity requires further study. Furthermore, some researchers measured the permeability of plugs and crushed wet shales and found that the permeability values were negatively correlated with water content (Gao and Li, 2018; Achang et al., 2019). Wang and Yu (2020) found that the main reason for the decrease in permeability of wet shale is the decrease in effective porosity due to the occupation of shale pore space by water. However, the impact of mineral and total organic carbon (TOC) contents on wet shale matrix permeability are currently unknown and need to be investigated.

Commonly used methods for matrix permeability measurement include the Gas Research Institute (GRI) technique (Cui et al., 2009; Tinni et al., 2012), and the pulse-decay method (Heller et al., 2014). The GRI method has the advantages of readily available and easily prepared test samples and convenient and rapid experimental operation (Cui et al., 2009). However, this method measures matrix permeability only under normal pressure conditions (Peng and Loucks, 2016; Achang et al., 2017). While this restriction can be overcome via the pulse decay method since it can evaluate shale matrix permeability under higher confining pressure conditions, which makes the method susceptible to influence of fractures (Heller et al., 2014; Peng et al., 2019). Another method that is used to measure shale matrix permeability is the mercury injection capillary pressure (MICP) technique (Gao and Hu, 2013; Sun et al., 2017; Yang et al., 2019). This method focuses on a characterization of the permeability at different connected pore network. Considering the fact GRI, pulse-decay, and MICP methods have separate measurement

limitations, a comprehensive characterization of shale matrix permeability is achieved if they are used altogether.

Thus, this study attempts to utilize a combination of these techniques with water vapor adsorption (WVA) to analyze the effects of pore connectivity and water saturation on deep shale matrix permeability. First, apparent permeability in different directions was measured by the pulse-decay method. Then GRI matrix permeability with different water saturations, and MICP technique was utilized to calculate permeability. Next, the effect of pore connectivity on permeability and the link between MICP permeability and apparent and matrix permeability are discussed by comparing permeabilities from these three sources. Finally, combined with WVA, the reasons for the decrease in permeability of the wet shale matrix was investigated. Ultimately, this study establishes an effective permeability evaluation index for shale gas reservoirs, which can enable us for sweet spot selection and production prediction in shale gas reservoirs globally.

## 2. Samples and methods

### 2.1 Geological setting and samples

The YT3 well is drilled in a deep shale gas reservoir in the Yichang area of the middle Yangtze in Southern China. The four shale samples selected for the study were collected from depths of 3530 to 3565 m in the Wufeng-Longmaxi Formation. The YT3 well (Fig. 1) is located within the Dangyang Synclinorium. The western uplift of the Dangyang Synclinorium is the Huangling anticline, and the eastern uplift is the Lexiangguan-Qianjiang anticlinorium, with a nearly north-south strike. From these four samples one shows the development of lamina, the second one lesser degree of micro-fractures development, the third one is exhibiting the presence micro-fractures and the fourth one, neither lamina nor fractures. Selection of these samples was based on the development of common lamina and fractures in shale reservoirs and their variability. Table 1 shows the depth, helium porosity, and TOC content of the samples, along with the mineralogical information obtained via X-ray diffraction.

The sample sizes required for testing varied between methods, but to ensure test specimens were representing one sample, proper homogenization was followed and aliquots were from the same sample piece. To be more specific, a cube with a length of 1.5 cm was first cut from each sample core for vertical and parallel laminar apparent permeability measurements, while another cubic piece with a length of 1 cm was cut adjacent to the first one for MICP testing. Matrix permeability measured by the GRI method is correlated with particle size, thus a sample with mesh size of 20-35 was crushed to better represent the matrix permeability (Cui et al., 2009; Achang et al., 2017). Since the samples tested by MICP cannot be reused, the 20-35 mesh size crushed specimens were used for the GRI method for matrix permeability measurements while they were obtained from the cubic piece of 1.5 cm length. This way ensured the results of all three methods can be truly represent one single sample to characterize the apparent permeability, MICP, and matrix permeability of it for better comparisons.

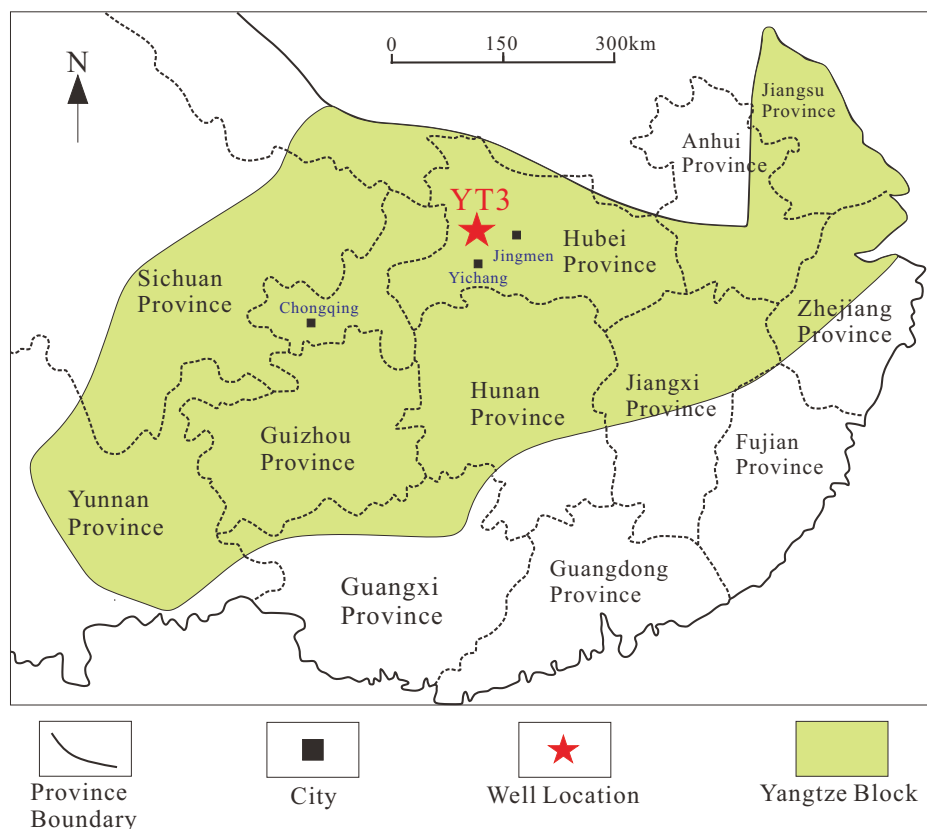


**Fig. 1.** Location map of the sampled well in the middle Yangtze region of China (modified by Xin et al., 2020).

**Table 1.** Basic properties of four YT3 shale samples.

Sample	Depth (m)	Quantitative analysis of whole-rock minerals (wt. %)						TOC (wt. %)	Porosity (%)
		Quartz	Plagioclase	Calcite	Dolomite	Pyrite	Clays		
YT3-21	3533.4	26.1	12.2	0	0	1.0	60.7	0.45	2.0
YT3-26	3552.45	42.3	13.2	1.5	2.8	1.9	38.3	2.79	1.9
YT3-29	3559.65	51.7	11.8	1.1	1.6	2.5	31.3	4.19	2.5
YT3-31	3565.36	69.1	5.6	0	0	0	25.3	1.78	1.4

## 2.2 Apparent permeability

The apparent permeability was measured using a PorePDP-200 instrument and helium under a confining pressure of 10 MPa and temperature of 35 °C. The method prescribed by Pan et al. (2015) was used to measure the apparent permeability in parallel and vertical laminar directions. First, the shale sample was machined into a cubic shape in 1.5 cm using a wire cutting machine. Next, a 2.5 cm diameter membrane of cylindrical photo polymer material was fabricated using 3D printing technology. Finally, permeability testing was performed by assembling cubic samples with the fabricated membranes to simulate standard core plug samples (Fig. 2). Permeability can be measured in different directions ( $X$ ,  $Y$ ,  $Z$ ) by rotating the cubic piece about its individual axes.



**Fig. 2.** 3D-printed polymer membrane with cubic sample.

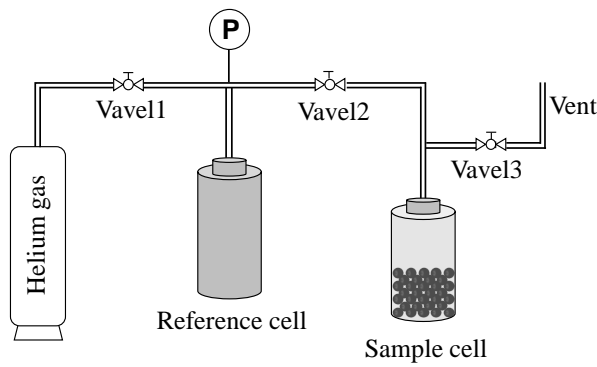


Fig. 3. Schematic diagram of SMP-200.

### 2.3 GRI matrix permeability

The matrix permeability of the shale was measured using a SMP-200 apparatus following the GRI method with helium and shown in Fig. 3 (Luffel and Guidry, 1989, 1992). A pressure decay leak test is required for the equipment before testing to ensure that the instrument is tightly sealed and that the environmental temperature is maintained at a constant 35 °C. During the test, the gas was drained from the reference and sample cells, then valves 2 and 3 are closed and valve 1 is opened to fill the sample cell with helium gas to an initial pressure of 200 psi. Finally, closing valve 1 and opening valve 2 will release the gas into the sample cell and the pressure-time data was recorded for 2000 seconds. Permeability values were obtained by curve fitting using the pressure-decay software that Core Laboratories provides with the SMP-200.

First, the 20–35 mesh crushed shale was dried at 110 °C for 48 h to remove the water. Next, the samples were transferred into a dry constant temperature chamber maintained at 35 °C for 2 h to equilibrate the sample temperature to 35 °C. The matrix permeability of the sample in the dry state was tested. Then, the samples were placed in a constant temperature chamber at 35 °C and absorbed water at six relative humidities ( $\beta$ ) (11.3%, 23%, 32.7%, 57.5%, 68.8% and 75.2%) in sequence until saturation. The samples were tested once for matrix permeability after saturation at each relative humidity.

### 2.4 MICP

The Micromeritics AutoPore IV 9520 test apparatus can provide a mercury intrusion pressure range of 5-60,000 psi (0.034-413 MPa), and can measure pore throat diameters of 36  $\mu\text{m}$  to 2.8 nm. The 1  $\text{cm}^3$  cubic sample was dried at 60 °C for 48 h before testing. To allow a more accurate recording of the intrusion volume of mercury in the specimen, the test was performed using a 0.096 ml stem penetrometer.

MICP investigates multiple connected pore networks in shale via threshold pressure values obtained from logarithms of the difference between intruded mercury volume and intrusion pressure. This is because each threshold pressure represents the maximum intrudable pore-throat size for a connected pore network (Hu et al., 2017). The inflection points in the low-pressure region respond to the microfracture system and the micrometer-diameter connected pore network in the sample.

The high-pressure region represents the pore connected network in the nm-scale shale matrix. The permeability of this connected pore network can be calculated using the Katz-Thompson method (Katz and Thompson, 1986, 1987), Eq. (1):

$$k = \frac{1}{89} \frac{L_{\max}^3}{L_c} \phi S(L_{\max}) \quad (1)$$

where  $k$  is the absolute permeability,  $\mu\text{m}^2$ ;  $L_{\max}$  is the pore throat diameter when the hydraulic conductivity value is at its maximum,  $\mu\text{m}$ ;  $L_c$  is the critical pore throat diameter corresponding to the critical pressure when mercury completely spans (percolates) the sample,  $\mu\text{m}$ ;  $\phi$  is porosity, %; and  $S(L_{\max})$  is the mercury saturation at  $L_{\max}$ , %.

The effective tortuosity ( $\tau$ ) is an important parameter for characterizing the pore connectivity, and can be obtained using Eq. (2):

$$\tau = \sqrt{\frac{\rho}{24k(1 + \rho V_{tot})} \int_{r_{c,\min}}^{r_{c,\max}} \eta^2 f_v(\eta) d\eta} \quad (2)$$

where  $\rho$  is the bulk density,  $\text{g}/\text{cm}^3$ ;  $V_{tot}$  is the total intruded mercury volume,  $\text{mL}/\text{g}$ ; and  $\int_{r_{c,\min}}^{r_{c,\max}} \eta^2 f_v(\eta) d\eta$  is the pore throat volume probability density function.

### 2.5 Nitrogen and water vapor adsorption/desorption

$\text{N}_2$  adsorption experiments were performed using the Quantachrome Autosorb-iQ3 test apparatus which allows the quantitative analysis of pores with diameters smaller than 100 nm. Crushed shale (35–80 mesh) was oven dried at 110 °C for 5 h before being degassed and adsorbed at 77 K. As adsorbate-adsorbate interactions are considered in the density functional theory (DFT) model (Lastoskie et al., 1993) and the DFT model fits the isotherms of each sample well, the DFT model was used to analyze the pore size distribution (PSD) of 1.4–50 nm.

The same shale particles, dried at 110 °C for 48 h were tested for isothermal WVA using a Quantachrome Aquadyne DVS at an relative humidity range between 2% and 95% and 35 °C constant temperature. It is important to note that pre-test 2% relative humidity within the chamber was achieved via nitrogen at a flow rate of 100–150  $\text{cm}^3/\text{min}$  before the experiment was conducted. The experiment sequentially recorded the change in the mass of the sample with a balance accuracy of 0.1  $\mu\text{g} \pm 1\%$  during the adsorption and desorption processes. In addition, the conditions for sample adsorption/desorption equilibrium at a set relative humidity value involved a sample mass change of less than 0.001 %/min.

## 3. Results

### 3.1 Permeability

#### 3.1.1 Apparent permeability in different directions

The apparent permeability of the samples was tested at a confining pressure of 5 MPa and an upstream pressure of 1.38 MPa (200 psi). Results obtained (Table 2) reveal permeability parallel to the bedding plane of rang from  $8.21 \times 10^4$  to less than 1 nD, while permeability vertical to the bedding plane

**Table 2.** Permeability by the MICP, pulse-decay, and GRI methods.

Sample	MICP				Apparent permeability (nD)		GRI matrix permeability (nD)
	Threshold pressure (MPa)	Threshold pore-throat diameter (nm)	Permeability (nD)	Effective tortuosity	Parallel	Vertical	
YT3-21	0.18	6951.63	$6.56 \times 10^5$	4.83	$7.34 \times 10^4$	<1	$4.27 \times 10^{-2}$
	1.23	1012.07	$3.42 \times 10^4$	14.27			
	19.29	64.64	116.20	244.67			
	234.38	5.32	1.39	2231.94			
	406.59	3.06	0.42	2749.82			
YT3-26	0.16	6963.71	$3.73 \times 10^6$	6	52	<1	0.12
	48.18	25.88	39.53	1845.22			
	155.09	8.04	2.71	7041.71			
	406.61	3.01	1.48	9513.94			
YT3-29	0.17	7546.43	$1.21 \times 10^6$	7.2	$8.21 \times 10^5$	<1	0.25
	1.92	648.17	$1.68 \times 10^4$	61.09			
	61.99	20.12	22.62	1663.25			
	155.08	8.04	2.52	4979.24			
YT3-31	372.16	3.35	1.27	7015.39	<1	<1	$2.65 \times 10^{-2}$
	0.2	7543.01	$3.73 \times 10^5$	4.31			
	61.99	20.12	11.36	1159.4			
	155.08	8.04	1.25	3493.8			
	406.59	3.06	0.67	4762.09			

was less than 1 nD.

### 3.1.2 GRI matrix permeability at different water saturations

The ratio of pore volume occupied by water to the total pore volume is represented by shale water saturation (S) (Wang and Yu, 2020), which along with GRI matrix permeability corresponding to the shale water absorption at different relative humidity are shown in Table 3. The latter is observed to decrease exponentially with increasing water saturation (Fig. 4).

Studies have observed that water molecule adsorption mechanism in shale pores differs at low relative humidity (0–23%) and medium relative humidity (23%–75.2%) conditions (Xu et al., 2020). Thus, the matrix permeability loss rate ( $\alpha$ ) was proposed to better analyze the effect of each adsorption mechanism on the matrix permeability (Gao and Li, 2018). The matrix permeability loss rate was calculated for the two stages according to Eq. (3), and the results are listed in Table 4.

$$\alpha = \frac{k_{\beta=i1} - k_{\beta=i2}}{k_{\beta=i1}} \quad (3)$$

where  $k_{\beta=i}$  is the matrix permeability at  $\beta = i$ , %.

From Table 4, it is observed that the rate of matrix perme-

ability loss differs with relative humidity for each sample, with the highest permeability loss rate for sample YT3-21 and the lowest for YT3-29 at all relative humidity values. For the low relative humidity shale samples, the permeability loss ranged from 59.25% to 15.82%. The permeability loss for YT3-21 was 59.25%; much higher than other three samples. For the

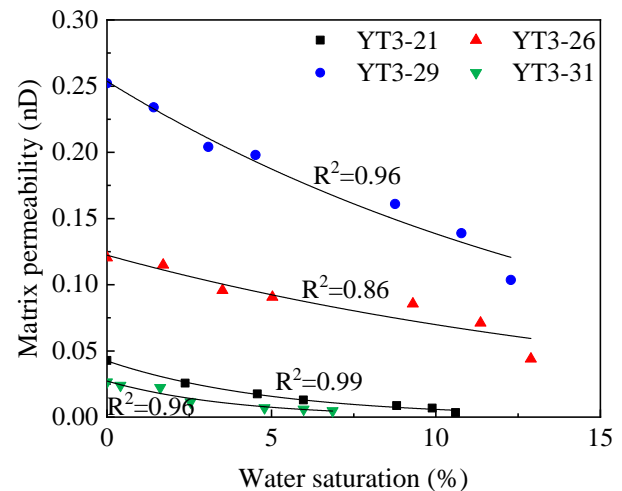


**Fig. 4.** Relationship between water saturation and GRI matrix permeability for the studied shale samples.

**Table 3.** Water saturation and GRI matrix permeability of each relative humidity.

Relative humidity (%)	YT3-21		YT3-26		YT3-29		YT3-31	
	Saturation (%)	Permeability ( $\times 10^{-2}$ nD)	Saturation (%)	Permeability ( $\times 10^{-2}$ nD)	Saturation (%)	Permeability ( $\times 10^{-2}$ nD)	Saturation (%)	Permeability ( $\times 10^{-2}$ nD)
0	0	4.27	0	12.58	0	0.25	0	2.65
11.3	2.38	2.56	1.71	11.24	1.42	0.23	0.41	2.40
23	4.57	1.74	3.51	9.57	3.08	0.20	1.62	2.23
32.7	5.97	1.29	5.03	9.07	4.52	0.19	2.54	1.13
57.5	8.81	0.86	9.30	8.55	8.76	0.16	4.79	0.70
68.8	9.89	0.68	11.36	7.12	10.78	0.14	5.98	0.59
75.2	10.60	0.34	12.89	4.40	12.28	0.10	6.86	0.48

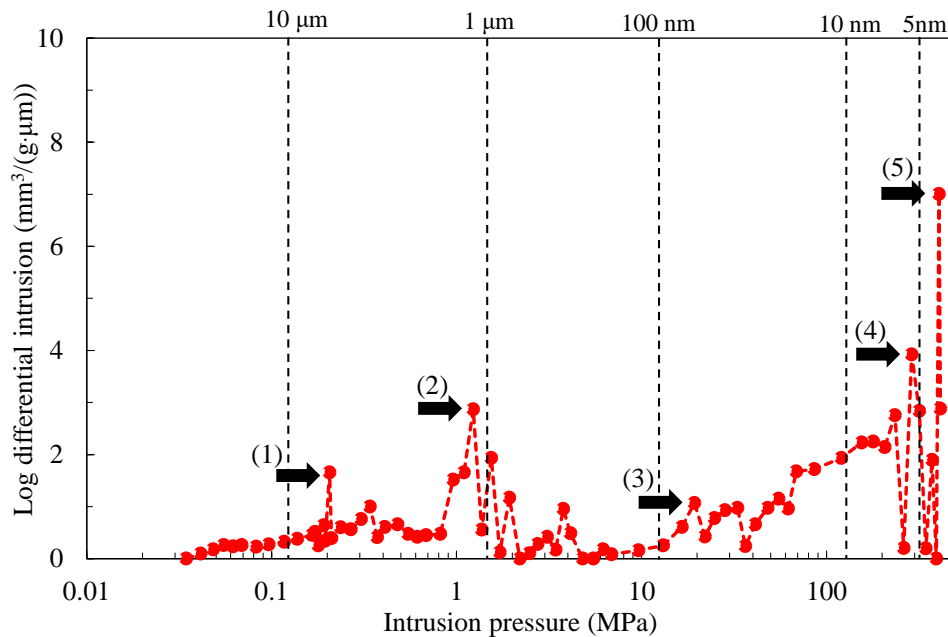


**Fig. 5.** Log differential intrusion versus intrusion pressure for sample YT3-21.

**Table 4.** Matrix permeability loss rate value of each relative humidity range.

Relative humidity (%)	Matrix permeability loss rate (%)			
	YT3-21	YT3-26	YT3-29	YT3-31
0-23	59.25	20.46	19.07	15.82
23-75.2	80.65	54.08	49.26	78.64
0-75.2	92.11	63.47	58.94	82.02

high relative humidity shale samples, the permeability loss varied from 80.65% to 49.26%, with YT3-21 and 31 showing a decrease of 80.65% and 78.64%, respectively.

### 3.1.3 MICP permeability

The Katz-Thompson method (Eq. (1)) was used to calculate the permeability of the connected pore network for different shale scales. Considering the YT3-21 as an example (Fig. 5),

inflection points (1) and (2) are in the low-pressure region, illustrating two different connected pore networks on the micron scale of this sample. The low-pressure region inflection points (1) and (2) represent the characteristics of microfracture/laminar structures and micron-scale connected pore network flow channels in the samples. The high-pressure region was divided into three connected pore networks: 2.8–5.0 nm, 5–10 nm, and 10–100 nm according to Gao and Hu (2013). These threshold pressure points are indicated by inflection points (3) through (5) on Fig. 5.

The connected pore network permeability, the corresponding critical pore throat diameter, and effective tortuosity (Table 2) were calculated using Eqs. (1)-(2). The values of critical pore throat diameter and permeability decreased rapidly by one order of magnitude with the increase in threshold pressure. The trend of the permeability of each connected pore network is shown in Fig. 6. As the scale of the connected pore network decreased, the permeability decreased significantly as well. The connected pore network permeability in the low-pressure

region samples ranged from  $3.73 \times 10^6$  to  $1.68 \times 10^4$  nD, and the effective tortuosity from 4.31 to 14.27. For the high-pressure region, the critical pore throat diameter of sample YT3-21 was 64 nm in the 10–100 nm pore network, which is much larger than the other three samples. Conversely, the critical pore throat diameter of 5.32 nm in the 5–10 nm pore network was much smaller compared to the other three samples. This may be due to the lower TOC and higher clay

content of YT3-21. The organic pores of the sample were not developed, and the pores were mainly inorganic mineral pores with large diameter.

## 3.2 Pore structure

### 3.2.1 MICP

Mercury intrusion and extraction curves for four shale samples from an initial pressure of 5–60,000 psi (0.034–413 MPa) are presented in Fig. 7(a). The cumulative volume of intruded mercury in samples YT3-26 and YT3-29 increased rapidly when the intrusion pressure was raised to 10,000 psi. This indicates that the sample pore throats were very well developed. The cumulative volume of intruded mercury increased to some extent during the extraction phase, which was caused by the compressibility of the mercury in the penetrometer.

The porosity, median pore-throat diameter, average pore-throat diameter, and pore-throat diameter distributions obtained by the MICP experiments are shown in Table 5 and Fig. 7(b). The pore throats connected to the pores of the samples were mainly distributed between 2.8 and 20 nm and between 8 and 30  $\mu\text{m}$ . In the 2.8–20 nm interval, the connected pore volumes of samples YT3-26 and 29 were higher than YT3-21 and 31 samples in the same interval. Finally, in the 8–30

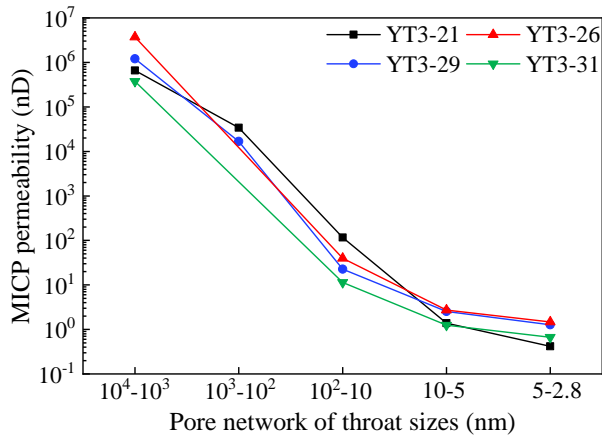


**Fig. 6.** MICP permeability of connected pore networks at different scales.

**Table 5.** Pore structure characteristics from the MICP test.

Sample	Bulk density (cm <sup>3</sup> /g)	Pore surface area (m <sup>2</sup> /g)	Porosity (%)	Median pore-throat diameter (nm)	Average pore-throat diameter <sup>a</sup> (nm)
YT3-21	2.67	1.40	1.06	19.71	11.34
YT3-26	2.59	2.78	1.66	15.72	9.20
YT3-29	2.54	2.30	1.45	16.92	9.95
YT3-31	2.58	1.12	0.72	17.89	10.00

<sup>a</sup>Average pore-throat diameter was calculated as  $4V/A$  ( $V$  = pore volume;  $A$  = pore area) based on the assumption of cylindrical pores.

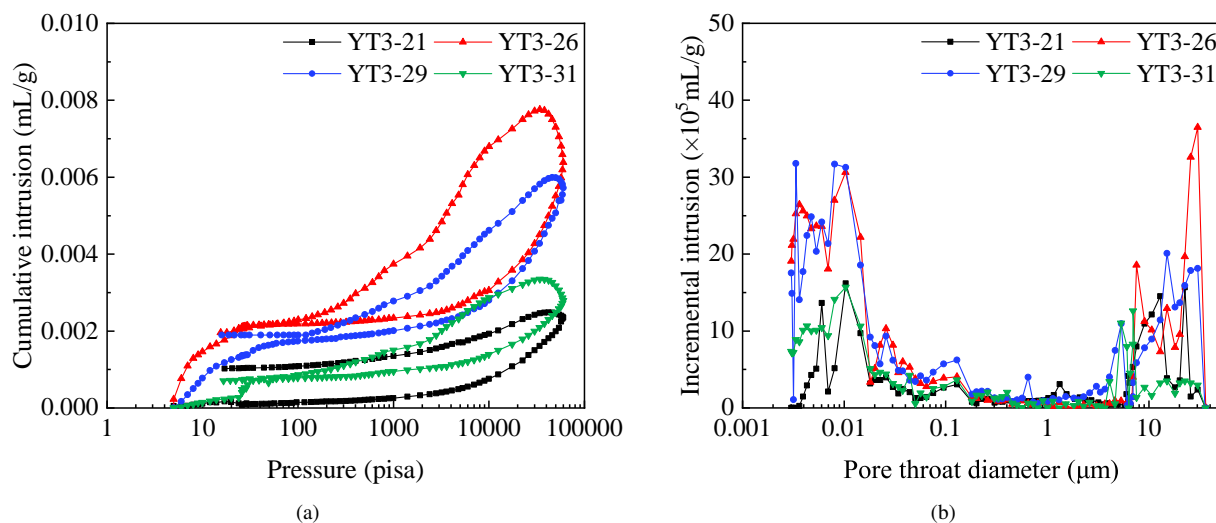


**Fig. 7.** (a) MICP intrusion curves and (b) pore-throat size distribution of studied shale samples.

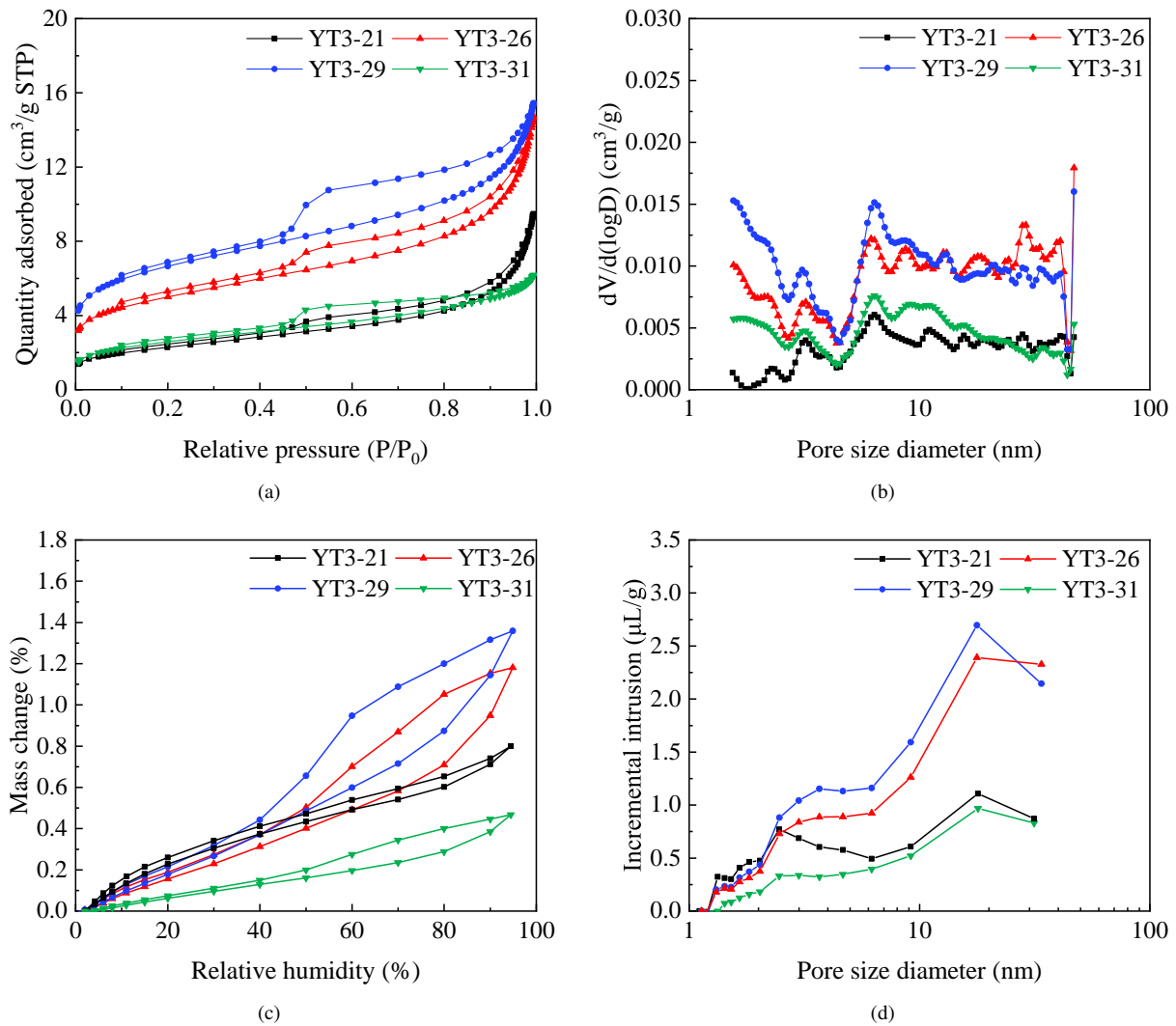


**Fig. 8.** (a, b) N<sub>2</sub> adsorption/desorption isotherms and PSD for the studied shale samples and (c, d) water vapor adsorption/desorption isotherms and PSD for the studied shale samples.

μm range, YT3-31 had the least volume of connected pores. However, sample YT3-26 had a significant increase in the amount of intruded mercury at 20 μm.

### 3.2.2 Nitrogen and water vapor adsorption/desorption

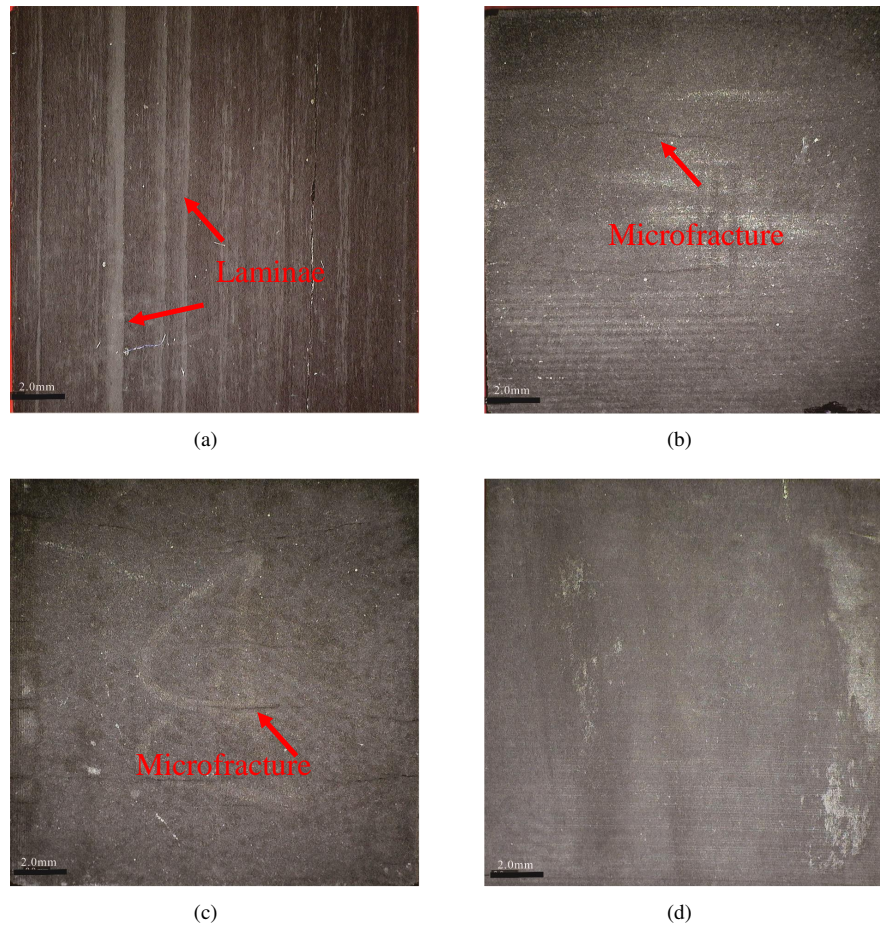
The sample nitrogen absorption/desorption curves are presented in Fig. 8(a). Each curve has hysteresis loops of different sizes caused by phase changes (capillary coalescence phenomenon) and pore blockage (ink-bottle effect) at reduced relative pressure (Hu et al., 2017). The adsorption amounts of samples YT3-26 and 29 were significantly more than YT3-21 and 31. When the relative pressure approached to 1, the amount of water vapor adsorption in samples YT3-21, 26, and 29 increased rapidly and did not reach adsorption saturation, indicating that connected large-diameter pores and microfractures exist in the shale samples (Nguyen et al., 2013).

Fig. 8(b) presents the PSD distribution obtained by the DFT model. Samples YT3-26, 29, and 31 have different degrees of pore development at 1.5–3 nm. This figure shows

a notable decrease in the curve at 4.5 nm. The curve at 6–50 nm is approximately horizontal, indicating that the pores are well developed and provide the main pore volume across the mesoporous range of the sample.

Fig. 8(c) exhibits the results of water vapor adsorption for the four samples. The maximum and minimum values of the total adsorption mass change of water vapor were 1.35% (YT3-29) and 0.46% (YT3-31), respectively. When relative humidity was low, the rate of change of the mass from the total water vapor adsorption for samples YT3-21, YT3-26, and YT3-29 increased promptly, with the largest rate of mass change found in sample YT3-21. Though, with increasing relative humidity, the amount of water vapor adsorbed varied between samples. The rate of change of the total water vapor adsorption mass of YT3-21 quickly slowed, yet, the rate of mass increase for samples YT3-26 and YT3-29 remained high.

When water vapor is adsorbed, condensation begins in the small capillaries, while as the relative humidity increases, the water vapor condenses in the larger capillaries. Based on the



**Fig. 9.** Observation of laminate structure from sample photos: (a) YT3-21 the presence of laminae of different widths; (b, c) there are multiple microfractures on the surface of YT3-26, 29; and (d) no observable laminae or microfractures exist on the surface of YT3-31.

Kelvin equation (Fisher and Israelachvili, 1979; Zolfaghari et al., 2017b), the relationship between relative humidity and the pore radius ( $r_p$ ) of water condensation-filled capillaries is described with the following expression:

$$\ln \frac{1}{\beta} = \frac{2\gamma V_m \cos \theta}{RT r_p} \quad (4)$$

where  $V_m$  represents the water vapor molar volume, mL/mol;  $\gamma$  the surface tension,  $10^{-3}$  N/m;  $\beta$  the relative humidity, %;  $\theta$  the contact angle,  $R$  the gas constant, J/mol·K; and  $T$  the temperature, K.

Before capillary condensation, due to van der Waals forces, water molecules interact with the pore surface via multilayer adsorption, with the surface covered with a certain thickness of water film (Yang et al., 2020). According to Hasley's formula, the thickness of the water film formed due to van der Waals forces ( $t$ ) can be derived as:

$$t = 0.354 \left( \frac{-5}{\ln \frac{P}{P_0}} \right)^{\frac{1}{3}} \quad (5)$$

where  $P/P_0$  the relative pressure.

Thus, the pore radius ( $r$ ) obtained from water vapor ad-

sorption is:

$$r = r_p + t \quad (6)$$

Fig. 8(d) illustrates the distribution of pore size in relation to the incremental water intrusion. The amount of adsorption by YT3-31 in micropores smaller than 2 nm (relative humidity approximately 20%) was only one-third of other samples in the same pore size. The adsorption increments of samples YT3-26 and YT3-29 continued to increase quickly in the 2–30 nm mesopore range, while the adsorption increments of YT3-21 decreased until it followed a similar pattern of sample YT3-31.

### 3.3 Microfractures and laminae distribution

The microfractures and laminar structures of the samples were observed using a Dino-lite digital microscope. According to the observation photos, the YT3-21 lamina interface is clear and uneven in thickness (Fig. 9(a)). The laminae are tabular, continuous, and oriented parallel to each other. The surface laminae of YT3-26 and YT3-29 were not clearly developed (Figs. 9(b) and 9(c)). Microfractures on the surface of the samples developed along the laminae. Furthermore, the microfractures on the surface of YT3-29 are more densely

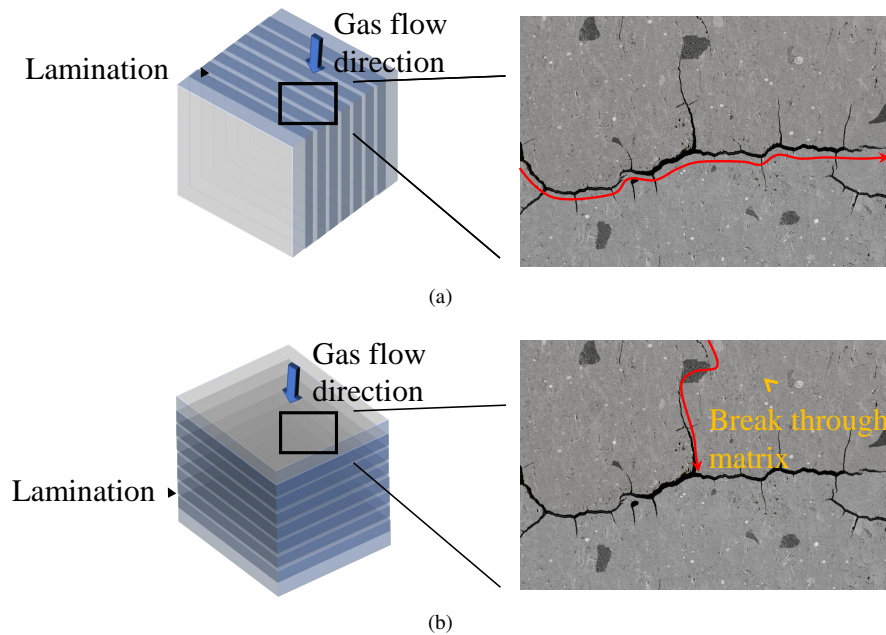


**Fig. 10.** Gas transport model, (a) gas flow from laminae microfractures; (b) gas flow from vertical laminae.

developed, whereas, YT3-31 had no obvious microfractures or laminae present on the surface (Fig. 9(d)).

## 4. Discussion

The permeability measured by these three methods mainly characterizes the connected pore networks of different sizes. Moreover, the apparent permeability measured by pulse-decay method at lower confining pressures mainly characterizes the micron-scale connected pore network. The matrix permeability obtained from 20-35 mesh size crushed sample measured by GRI method eliminates the effects of micro-fractures and characterizes the matrix connected pore network at the nanoscale. Ultimately, MICP permeability can define the connected pore network at different scales from micron to nanometer, thus it is used to compare with the apparent permeability and GRI matrix permeability.

### 4.1 Comparison of three permeability testing methods

A comparison of apparent permeability with MICP permeability of the micron-scale connected pore network (Table 3) reveals that apparent permeability of YT3-21 with laminae development and YT3-29 with microfractures development are similar to the MICP permeability. However, the apparent permeability of YT3-26 in the horizontal direction (i.e., parallel to the bedding plane) differs from the MICP permeability. These are inferred to the intrusion of mercury into connected pores of the sample from all directions during MICP measurements differing from the measurement of fluid propagation through the sample under confining pressure following conventional pulse-decay method.

Thus, for samples with developed laminae characterized by microfractures which become conduits for gas flow, the measured permeability represents the microfracture structure

(Fig. 10(a)). However, when measuring permeability in the direction vertical to the direction, where microfractures are less developed and gas flow needs to break through the matrix pore network, the measured permeability represents the matrix structure (Fig. 10(b)). This can also be observed via a correlation between apparent permeability and MICP permeability demonstrated by apparent permeability of YT3-26 in the parallel direction being much smaller than MICP permeability in the low-pressure region. This has happened since laminae and connected fractures are not developed in that particular direction. Thus, indicating a similarity to MICP permeability values for a 10–100 nm scale connected pore network. While lesser degree of permeability is also observed in a sample (YT3-31) with no development of laminae nor microfractures. This is important because studies have noted that under higher confining pressures, shale samples with developed microfractures are characterized by permeability similar to the matrix permeability of unfractured samples due to such pressures eliminating the effects of microfractures on permeability (Yang et al., 2019).

The ratio of MICP permeability for the matrix connected pore network to GRI matrix permeability explains that the MICP matrix permeability in the high-pressure region is tens or even hundreds of times higher than the one obtained by the GRI method. The GRI method uses crushed samples, which eliminates the effect of micron scale fractures. However, Achang et al. (2017) observed that permeability measurements using the GRI method are affected by nano-fractures. Moreover, the GRI method currently lacks a uniform calculation standard, and there are obvious discrepancies in the results measured by various methods (Cui et al., 2009; Heller et al., 2014; Achang et al., 2017). Hu et al. (2017) explained discrepancy between the two methods is due to the laminar and microfracture structures of the samples.

## 4.2 Effect of pore connectivity on permeability

Shale micrometer-scale pore network connectivity is a principal factor affecting permeability (Davudov et al., 2020; Ghasemi et al., 2020), with laminae microfractures being the main pathways for gas transport (Achang et al., 2017; Peng et al., 2019; Zhao et al., 2020). In the shallow Longmaxi and Niutitang formations, the MICP permeability of connected pores at different scales varies by several orders of magnitude, and the MICP permeability of matrix-connected pores is in the nano-Darcy range (Yang et al., 2019).

In the MICP test, mercury first intrudes into microfractures and then into the matrix-connected pores as the pressure rises (Zhao et al., 2020). The MICP permeability of the 1–10  $\mu\text{m}$  connected pore network for sample YT3-31 was smaller than other samples (Figs. 6). Microfractures have a significant effect on permeability, and investigations have found that the permeability of microfracture-developed samples is greater than samples lacking such features (Ma et al., 2016a). Thus, in this study, because fractures and laminae were present in samples YT3-21, YT3-26, and YT3-29 (Figs. 9(a), 9(b), and 9(c)), their apparent permeability in the direction parallel to the laminae direction was significantly higher than that of YT3-31 which has the smallest 1–10  $\mu\text{m}$  connected pore network permeability (Table 2). However, the apparent permeability of YT3-21, YT3-26, and YT3-29 in the direction, perpendicular to the bedding planes was less than 1 nD, and there were significant differences between the apparent permeability in these two directions. Only sample YT3-31 (Fig. 9(d)), where fractures and laminae are not developed, had permeability less than 1 nD in both directions. Ma et al. (2016a) also found that the permeability anisotropy of fracture-developed samples was greater than samples missing such features. This indicates that the development of fractures and laminae contributes drastically to apparent permeability and is a major reason for the strong anisotropy of permeability parallel and perpendicular to the laminae.

The connectivity of organic and inorganic pores in the shale matrix connected to the pore network govern on the permeability of the shale. In this study, pore throat diameter for the 10–100 nm pore network was measured by MICP as being smaller than 20 nm. This observation is also supported by nitrogen adsorption experiments indicating that sample pore diameters were substantially developed from 10–50 nm. Thus, meaning that a large number of pores with diameters greater than 20 nm in the YT3 shale are connected by pore throat diameters smaller than 20 nm. Previous studies on the shales from the Wufeng-Longmaxi Formation also confirmed the presence of “ink bottle” pores (Wang et al., 2016).

Pore diameter affects gas transport in the matrix pores. As the formation pressure increases, the larger pores of the shale are affected by compaction. This shifts the pore geometry towards smaller pores and lowers the permeability of the shale matrix (Qu et al., 2016). In this study, the role of compaction can be verified by the MICP permeability and critical pore throat diameter of YT3-21 being the largest for the 10–100 nm pore network (Table 2). This is due to the lower TOC in this sample which has led to having mineral

pores mainly of inorganic nature of inter- and intra-grain type. When organic matter content exceeds a certain level, the overall plastic strength of the rock increases and it will become more susceptible to compaction (Milliken et al., 2013), which results in overall smaller critical pore throat diameters. This also explains the observation of higher MICP permeability in 2.8–10 nm connected pore networks for samples with higher TOC content (e.g., YT3-26 and YT3-29). Thus, the connected pore network of shales analyzed in this study is mostly controlled by organic pores.

## 4.3 Effect of water saturation on matrix permeability

WVA in shale pores occurs in three main stages: Monolayer adsorption, multilayer adsorption, and capillary coalescence (Tang et al., 2017; Sang et al., 2019). In this study, the decrease in matrix permeability at different adsorption stages varied, and their matrix permeability loss rate are listed in Table 2. Based on the characteristics of each adsorption stage, the reasons and factors influencing the decrease in matrix permeability are discussed.

When relative humidity is relatively low, monolayer adsorption occurs because of strong hydrogen bonds between the water molecules and hydrophilic pore walls (clay minerals), with most water molecules being preferentially adsorbed on the main adsorption sites and epoxy functional groups (Fig. 11(a)) (Li et al., 2016). During the relatively lower relative humidity stage (0–20%), inorganic pores of clay minerals are more hydrophilic than the organic matter, hence water molecules preferentially would occupy the hydrophilic sites of clay minerals. A positive correlation was found between shale water vapor adsorption and clay content (Fig. 12(a)). Zolfaghari et al. (2017a) observed that the adsorption of water molecules in shale on clay mineral processes is the main mechanism of water absorption in shale at lower relative humidity. The clay in the shale matrix absorbs water and swells, thus occupying the pore channel space and reducing the effective pore channel diameter, resulting in a weakened gas transport capacity. In contrast, hydrophobic organic pores have weak interactions with water molecules and occupy a very limited space. Therefore, a good positive relationship was established between matrix permeability loss rate and shale clay content at the relatively lower relative humidity stages (0–20%) (Fig. 12(b)).

As the relative humidity increased ( $20\% < \beta < 75\%$ ), the main adsorption sites on the surface of the hydrophilic pore walls are occupied by water molecules that continue to be adsorbed. In addition, in the hydrophobic organic pore space, some water clusters gradually start to form, which occupy part of the pore volume for gas transport (Fig. 11(b)) (Ryan, 2006). With the gradual increase in the water film thickness on the pore walls, the spaces in the micropores and small-diameter pore throats become completely occupied by water, and condensation and water-locking effects would occur. This hinders gas transport and leads to a further decrease in matrix permeability.

In the multilayer adsorption phase, the matrix permeability

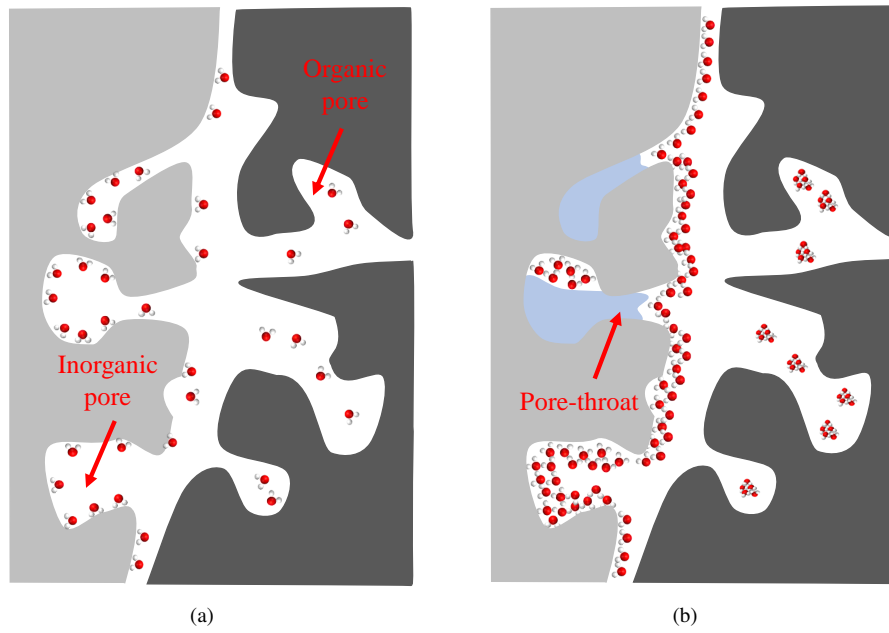


**Fig. 11.** Water adsorption and distribution characteristics in complex shale pores at different relative humidity values (modified by Sang et al., 2019): (a) Monolayer adsorption at a low relative humidity value, and (b) multilayer adsorption at an intermediate relative humidity value.

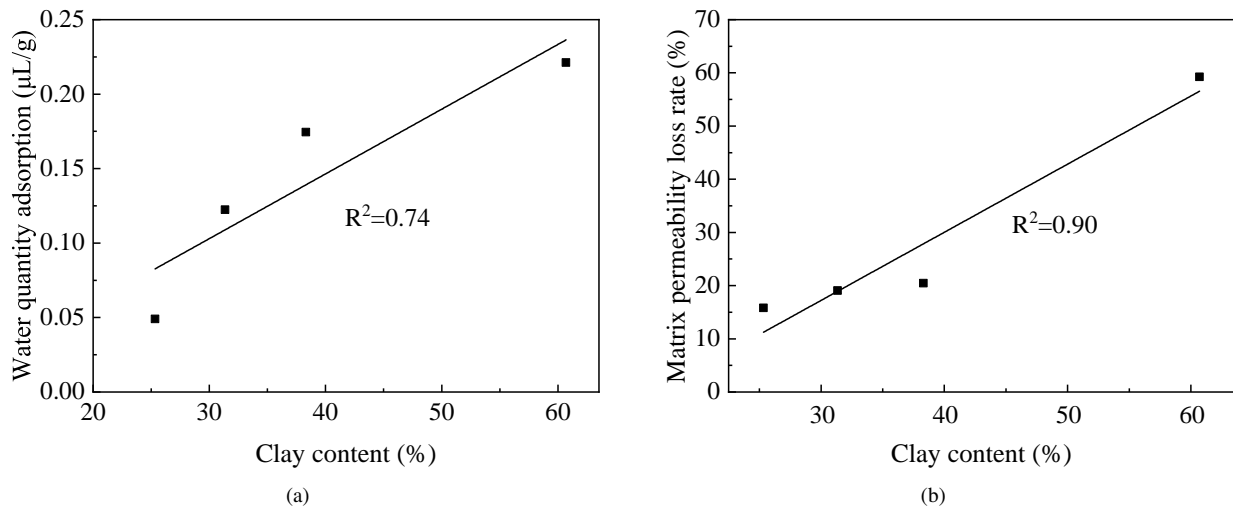


**Fig. 12.** (a) Relationship between clay content and water vapor adsorption and (b) relationship between clay content and matrix permeability loss rate ( $\alpha$ ) value ( $\beta = 0-20\%$ ).

loss rate values of samples YT3-21 and 31 with lower TOC content were as high as 80%, while the matrix permeability loss rate values of YT3-26 and 29 samples with higher TOC content were only approximately 50%. Organic pores were not developed in the shale samples with lower TOC content, and the pore network was mainly composed of inorganic pores. Water molecules generate thicker water film on the pore walls of inorganic pores, which reduces the effective radius of the pores. Some micro-pore throats with smaller pore sizes are completely "filled" (Lei et al., 2020; Xu et al., 2020). This results in poor connectivity in the inorganic pore

network, which obstructs the expansion and transport of gas through the network. Organic pores are developed in the pore network of shales with higher TOC content, and are one of the main components of the shale pore network. The organic pore connectivity is excellent in the shales of the Wufeng-Longmaxi Formation in the Yangzi area, but the average pore size is small ( $< 50$  nm) (Ma et al., 2016b; Chen et al., 2021). Water molecules form water clusters in the micro-organic pores, can occupy part of the pore spaces. However, some organic pores and channels remain free of water molecules (Sang et al., 2019; Yang et al., 2020). Therefore, the channels

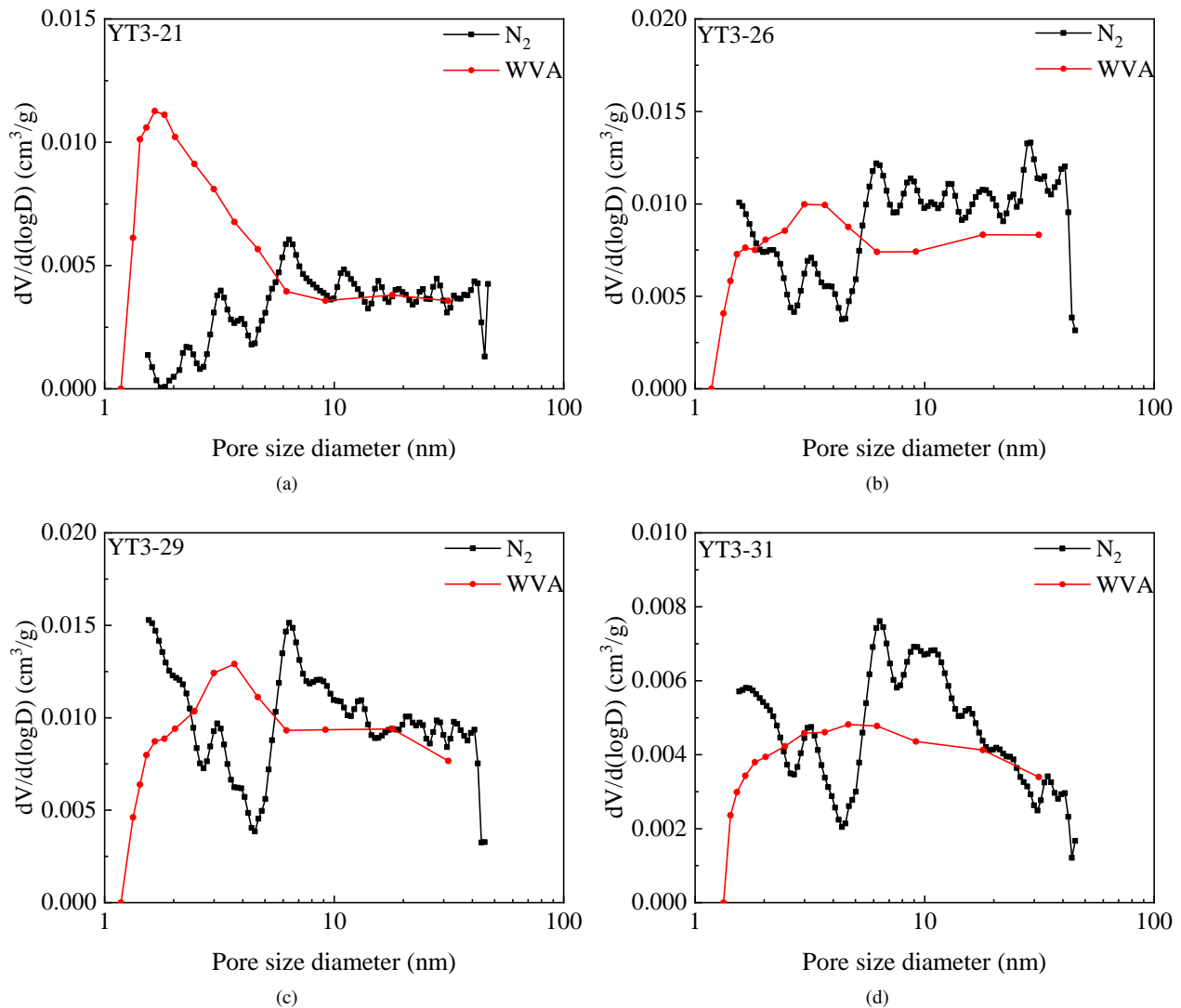


**Fig. 13.** Comparison of pore size distribution obtained from water vapor adsorption and nitrogen adsorption for the YT3 shales.

of the hydrophobic organic pore network remained connected, ensuring the diffusion and transport of gas.

In the process of WVA, the diameter of the pores filled by water molecules becomes increasingly larger as the relative humidity increases. Water completely occupies only micropores smaller than 10 nm under higher relative humidity conditions (Wang and Yu, 2020). The water vapor adsorption curve is significantly higher than nitrogen adsorption for pores in the 2–5 nm interval. For pores in the 2–5 nm region in samples with high clay content, the water vapor adsorption curve was significantly higher compared to the nitrogen adsorption (YT3-21), while the difference was minor in samples with less clay content (YT3-31) (Fig. 13).

The reason for this phenomenon is that polar water molecules are easily adsorbed on the surface of hydrophilic clay minerals and form clay-bound water in contact with cations on the clay surface (Chávez et al., 2001). These clay-bound waters gradually penetrated the interlayer micropores of clay minerals, where nitrogen barely penetrated. For pores

larger than 5 nm, the water vapor adsorption curve was slightly lower than the nitrogen adsorption curve. This is due to the increased spaces of organic pores, with condensation of water molecules occurring within the organic pores in the form of water clusters. Therefore, in the relative humidity range of 0–75%, water molecules mainly fill the pores and pore throats in the diameter range of 1.5–10 nm, indicating that water molecules mainly affect the pore network containing pores of 10 nm or less in diameter.

## 5. Conclusions

In this study, the influence of pore structure and water saturation on the permeability of the shale matrix was investigated. The test methods in this paper can be used on other shale formations, and the conclusions can also provide a reference for shallow shale formations in particular. The major conclusions are summarized as follows.

- 1) Pore connectivity is a key factor affecting permeability, even if laminae and crossing fractures are dominant

channels for gas transport. This is due to gas propagation through the shale matrix when these dominant flow conduits do not exist.

- 2) The MICP technique can evaluate the permeability of multiple connected pore networks. The smaller the scale of the connected pore network, the larger the effective tortuosity, the poorer the pore connectivity, and the lower the permeability would be.
- 3) The shale matrix permeability decreases exponentially with increasing water content. In the relative humidity range of 0–78%, water molecules mainly affect the pore network containing pores/pore throats with diameters less than 10 nm. In the lower relative humidity stages ( $\beta < 23\%$ ), matrix permeability loss rate values were positively correlated with clay mineral content. As the relative humidity increased ( $23\% < \beta < 75\%$ ), matrix permeability loss rate values were smaller for shales with higher TOC content.

## Acknowledgement

The authors sincerely thank the National Natural Science Foundation of China (41802146, 41972156, and 41830431), the Science and Technology Project of Heilongjiang Province (2020ZX05A01), and the Key Technology Research and Test for Effective Exploitation of Deep Shale Gas Program of CNPC of China (2019F-31), for their financial support.

## Conflict of interest

The authors declare no competing interest.

**Open Access** This article is distributed under the terms and conditions of the Creative Commons Attribution (CC BY-NC-ND) license, which permits unrestricted use, distribution, and reproduction in any medium, provided the original work is properly cited.

## References

- Achang, M., Pashin, J. C., Atekwana, E. A. The influence of moisture on the permeability of crushed shale samples. *Petroleum Science*, 2019, 16(3): 492-501.
- Achang, M., Pashin, J. C., Cui, X. The influence of particle size, microfractures, and pressure decay on measuring the permeability of crushed shale samples. *International Journal of Coal Geology*, 2017, 183: 174-187.
- Chávez-Páez, M., Workum, K. V., de Pablo, L., et al. Monte Carlo simulations of Wyoming sodium montmorillonite hydrates. *Journal of Chemical Physics*, 2001, 114(3): 1405-1413.
- Chen, K., Li, J., Tang, X., et al. Key geological factors for shale gas accumulation in the Wufeng-Longmaxi Formation in the central Yangtze area. *Natural Gas Industry B*, 2021, 8(1): 1-12.
- Cui, G., Liu, J., Wei, M., et al. Why shale permeability changes under variable effective stresses: New insights. *Fuel*, 2018, 213: 55-71.
- Cui, X., Bustin, A. M. M., Bustin, R. M. Measurements of gas permeability and diffusivity of tight reservoir rocks: Different approaches and their applications. *Geofluids*, 2009, 9(3): 208-223.
- Davudov, D., Moghanloo, R. G., Zhang, Y. Interplay between pore connectivity and permeability in shale sample. *International Journal of Coal Geology*, 2020, 220: 103427.
- Duan, W., Li, C., Luo, C., et al. Effect of formation overpressure on the reservoir diagenesis and its petroleum geological significance for the DF11 block of the Yinggehai Basin, the South China Sea. *Marine and Petroleum Geology*, 2018, 97: 49-65.
- Fisher, L. R., Israelachvili, J. N. Direct experimental verification of the Kelvin equation for capillary condensation. *Nature*, 1979, 277: 548-549.
- Gao, J., Li, Z. Water saturation-driven evolution of helium permeability in Carboniferous shale from Qaidam Basin, China: An experimental study. *Marine and Petroleum Geology*, 2018, 96: 371-390.
- Gao, Z., Hu, Q. Estimating permeability using median pore-throat radius obtained from mercury intrusion porosimetry. *Journal of Geophysics and Engineering*, 2013, 10(2): 025014.
- Ghasemi, F., Ghaedi, M., Escrochi, M. A new scaling equation for imbibition process in naturally fractured gas reservoirs. *Advances in Geo-Energy Research*, 2020, 4(1): 99-106.
- Guo, X., Li, Y., Borjigen, T., et al. Hydrocarbon generation and storage mechanisms of deep-water shelf shales of Ordovician Wufeng Formation–Silurian Longmaxi Formation in Sichuan Basin, China. *Petroleum Exploration and Development*, 2020, 47(1): 193-201.
- He, Z., Li, S., Nie, H., et al. The shale gas “sweet window”: “The cracked and unbroken” state of shale and its depth range. *Marine and Petroleum Geology*, 2019, 101: 334-342.
- Heller, R., Vermylen, J., Zoback, M. Experimental investigation of matrix permeability of gas shales. *AAPG Bulletin*, 2014, 98(5): 975-995.
- Hu, Q., Zhang, Y., Meng, X., et al. Characterization of micro-nano pore networks in shale oil reservoirs of Paleogene Shahejie Formation in Dongying Sag of Bohai Bay Basin, East China. *Petroleum Exploration and Development*, 2017, 44(5): 720-730.
- Katz, A. J., Thompson, A. H. Quantitative prediction of permeability in porous rock. *Physical Review B*, 1986, 34(11): 8179-8181.
- Katz, A. J., Thompson, A. H. Prediction of rock electrical conductivity from mercury injection measurements. *Journal of Geophysical Research*, 1987, 92(B1): 599-607.
- Lastoskie, C., Gubbins, K. E., Quirke, N. Pore size distribution analysis of microporous carbons: A density functional theory approach. *Journal of Chemical Physics*, 1993, 97: 4786-4796.
- Lei, G., Liao, Q., Chen, W., et al. Stress dependent gas-water relative permeability in gas hydrates: A theoretical model. *Advances in Geo-Energy Research*, 2020, 4(3): 326-338.
- Li, J., Li, X., Wang, X., et al. Water distribution characteristic and effect on methane adsorption capacity in shale clay. *International Journal of Coal Geology*, 2016, 159: 135-154.
- Li, J., Yang, Z., Wu, S., et al. Key issues and development

- direction of petroleum geology research on source rock strata in China. *Advances in Geo-Energy Research*, 2021, 5(2): 121-126.
- Luffel, D. L., Guidry, F. K. Core-analysis results: Comprehensive study wells, Devonian shale. Topical report, United States, May 1989.
- Luffel, D. L., Guidry, F. K. New core analysis methods for measuring reservoir rock properties of Devonian shale. *Journal of Petroleum Technology*, 1992, 44(11): 1184-1190.
- Ma, Y., Pan, Z., Zhong, N., et al. Experimental study of anisotropic gas permeability and its relationship with fracture structure of Longmaxi Shales, Sichuan Basin, China. *Fuel*, 2016a, 180: 106-115.
- Ma, Y., Zhong, N., Cheng, L., et al. Pore structure of the graptolite-derived OM in the Longmaxi Shale, southeastern Upper Yangtze Region, China. *Marine and Petroleum Geology*, 2016b, 72: 1-11.
- Milliken, K. L., Rudnicki, M., Awwiller, D. N., et al. Organic matter-hosted pore system, Marcellus Formation (Devonian), Pennsylvania. *AAPG Bulletin*, 2013, 97(2): 177-200.
- Nguyen, P. T., Do, D. D., Nicholson, D. Pore connectivity and hysteresis in gas adsorption: A simple three-pore model. *Colloids & Surfaces A Physicochemical & Engineering Aspects*, 2013, 437: 56-68.
- Pan, Z., Ma, Y., Connell, L. D., et al. Measuring anisotropic permeability using a cubic shale sample in a triaxial cell. *Journal of Natural Gas Science and Engineering*, 2015, 26: 336-344.
- Peng, S., Loucks, B. Permeability measurements in mudrocks using gas-expansion methods on plug and crushed-rock samples. *Marine and Petroleum Geology*, 2016, 73: 299-310.
- Peng, S., Ren, B., Meng, M. Quantifying the influence of fractures for more-accurate laboratory measurement of shale matrix permeability using a modified gas-expansion method. *SPE Reservoir Evaluation & Engineering*, 2019, 22: 1293-1304.
- Qu, H., Pan, Z., Peng, Y., et al. Controls on matrix permeability of shale samples from Longmaxi and Niutitang formations, China. *Journal of Natural Gas Science and Engineering*, 2016, 33: 599-610.
- Ryan, B. A discussion on moisture in coal implications for coalbed gas and coal utilization. *British Columbia Resource Development and Geoscience Branch, Summary of Activities*, 2006, 49: 139-149.
- Sang, G., Liu, S., Elsworth, D. Water vapor sorption properties of Illinois shales under dynamic water vapor conditions: Experimentation and modeling. *Water Resources Research*, 2019, 55(5): 7212-7228.
- Sun, M., Yu, B., Hu, Q., et al. Pore connectivity and tracer migration of typical shales in south China. *Fuel*, 2017, 203: 32-46.
- Sun, M., Zhang, L., Hu, Q., et al. Multiscale connectivity characterization of marine shales in southern China by fluid intrusion, small-angle neutron scattering (SANS), and FIB-SEM. *Marine and Petroleum Geology*, 2020, 112: 104101.
- Tan, Y., Pan, Z., Feng, X., et al. Laboratory characterisation of fracture compressibility for coal and shale gas reservoir rocks: A review. *International Journal of Coal Geology*, 2019, 204: 1-17.
- Tang, X., Ripepi, N., Valentine, K. A., et al. Water vapor sorption on Marcellus shale: Measurement, modeling and thermodynamic analysis. *Fuel*, 2017, 209: 606-614.
- Tinni, A., Fathi, E., Agarwal, R., et al. Shale permeability measurements on plugs and crushed samples. Paper SPE 162235 Presented at the SPE Canadian Unconventional Resources Conference, Calgary, Alberta, Canada, 30 October, 2012.
- Wang, M., Yu, Q. Comparing the permeability of dry and moisturized crushed shales determined by the dynamic process data of methane adsorption. *Journal of Hydrology*, 2020, 590: 125375.
- Wang, P. F., Jiang, Z. X., Chen, L., et al. Pore structure characterization for the Longmaxi and Niutitang shales in the Upper Yangtze Platform, South China: Evidence from focused ion beam-He ion microscopy, nano-computerized tomography and gas adsorption analysis. *Marine and Petroleum Geology*, 2016, 77: 1323-1337.
- Xu, R., Prodanović, M., Landry, C. Pore-scale study of water adsorption and subsequent methane transport in clay in the presence of wettability heterogeneity. *Water Resources Research*, 2020, 56(10): e2020WR027568.
- Yang, R., Hu, Q., He, S., et al. Wettability and connectivity of overmature shales in the Fuling gas field, Sichuan Basin (China). *AAPG Bulletin*, 2019, 103(3): 653-689.
- Yang, R., Jia, A., He, S., et al. Water adsorption characteristics of organic-rich Wufeng and Longmaxi Shales, Sichuan Basin (China). *Journal of Petroleum Science and Engineering*, 2020, 193: 107387.
- Zhang, J., Tao, J., Li, Z., et al. Prospect of deep shale gas resources in China. *Natural Gas Industry*, 2021, 41(1): 15-28. (in Chinese)
- Zhao, J., Hu, Q., Liu, K., et al. Pore connectivity characterization of shale using integrated wood's metal impregnation, microscopy, tomography, tracer mapping and porosimetry. *Fuel*, 2020, 259: 116248.
- Zolfaghari, A., Dehghanpour, H., Holyk, J. Water sorption behaviour of gas shales: I. Role of clays. *International Journal of Coal Geology*, 2017a, 179: 130-138.
- Zolfaghari, A., Dehghanpour, H., Xu, M. Water sorption behaviour of gas shales: II. Pore size distribution. *International Journal of Coal Geology*, 2017b, 179: 187-195.
- Zou, C., Zhao, Q., Cong, L., et al. Development progress, potential and prospect of shale gas in China. *Natural Gas Industry*, 2021, 41(1): 1-14. (in Chinese)